

Nanoindentation hardness anisotropy of alumina crystal: A molecular dynamics study

Kenji Nishimura,¹ Rajiv K. Kalia,² Aiichiro Nakano,^{2,a)} and Priya Vashishta²

¹Research Institute for Computational Science, National Institute of Advanced Industrial Science and Technology, Tsukuba, Ibaraki 305-8568, Japan

²Collaboratory for Advanced Computing and Simulations, Department of Physics and Astronomy, Department of Chemical Engineering and Materials Science, Department of Computer Science, University of Southern California, Los Angeles, California 90089-0242, USA

(Received 5 March 2008; accepted 20 March 2008; published online 23 April 2008)

Atomistic mechanisms of the initial stage of plasticity during nanoindentation are studied by molecular dynamics simulations for three surface orientations of alumina crystal. The simulations predict significant anisotropy and indentation depth dependence of the hardness value at the nanometer scale. The nanohardness anisotropy is found to arise from orientation-dependent dislocation activities. In the (0001) basal plane indentation, prism dislocations are emitted, followed by basal and pyramidal dislocations, to form massive subsurface defects; prism and pyramidal dislocations are emitted on (01 $\bar{1}$ 0) and (2 $\bar{1}$ $\bar{1}$ 0) prism plane indentations, respectively, to cause modest deformations. Stacking faults are also observed because these dislocations are extended to Shockley partial dislocations. © 2008 American Institute of Physics. [DOI: 10.1063/1.2913016]

Crystalline alumina (Al₂O₃) is a highly insulating, optically transparent, chemically stable, hard material with applications in many industrial fields ranging from metallurgical engineering to opto- and microelectronics. Nanoindentation is widely used to examine mechanical properties of materials at the nanometer scale,¹ and there have been a number of experimental studies^{2–6} of nanoindentation of alumina. These studies have shown that alumina, which is normally regarded as brittle (with the brittle-to-ductile transition temperature exceeding 1400 K), plastically deforms with discontinuous “pop-in” behavior at the nanometer scale in the load-displacement curve at much lower temperatures (even at room temperature).^{2–4} These studies also reveal an indentation size effect, i.e., the indentation hardness increases with decreasing penetration depth. Moreover, plastic deformation processes have been found to be highly sensitive to the crystallographic orientation of the surface.^{5–7}

Although scanning electron microscopy scanning tunneling microscopy, atomic force microscopy (AFM),⁸ and transmission electron microscopy (TEM) techniques have been applied to nanoindentation experiments, it is difficult to resolve detailed atomistic structures and processes associated with defects generated beneath the indenter. Atomistic simulations based on the molecular dynamics (MD) method have been previously employed to study subsurface deformations at the onset of plasticity,⁹ especially in indented metal thin films with single crystal,^{10,11} bicrystal,¹² and nanopolycrystal¹³ structures. Recently, MD simulations have also been applied to the study of nanoindentation in brittle ceramics such as silicon nitride^{14,15} and silicon carbide.^{16,17} However, little is known about the atomistic processes during nanoindentation on alumina, especially mechanisms responsible for plastic deformation processes underlying crystallographic anisotropy and indentation size effects.

This letter reports MD simulation results on atomistic-scale subsurface defect generation during nanoindentation of

α -crystalline alumina thin film for three indent surface orientations: (0001) basal, (01 $\bar{1}$ 0) prism, and (2 $\bar{1}$ $\bar{1}$ 0) prism planes. The hardness value estimated from the calculated load-displacement curve is consistent with experimental values at large indentation depths (h) but exhibits significant dependence on the surface orientation at indentation depth below $h \sim 15$ Å. Moreover, we observe distinct dislocation activities, including the emission and motion of basal, prism and pyramidal dislocations, beneath the indenter for the three different surface orientations. These results suggest that the nanohardness anisotropy is caused by the activation of different slip systems.

The interatomic potential used in our MD study consists of two- and three-body terms, which account for the effects of steric repulsion, charge transfer, electronic polarizability, van der Waals interaction, and covalent bonding. The calculated lattice constant, cohesive energy, elastic constants, and melting temperature are in good agreement with the experimental data. Similar potential forms have been used in MD studies of nanoindentation on silicon nitride^{14,15} and silicon carbide.^{16,17}

The simulated α -alumina substrate is a 200 Å cube, whose side surfaces are (0001) basal, (01 $\bar{1}$ 0) prism, and (2 $\bar{1}$ $\bar{1}$ 0) prism, planes, and it contains approximately 1×10^6 atoms. We have performed three simulations, where (0001), (01 $\bar{1}$ 0), and (2 $\bar{1}$ $\bar{1}$ 0) surfaces are indented, respectively. In each simulation, periodic boundary conditions are only applied in two directions perpendicular to the indent direction. The substrate thus has two free surfaces in the indent direction, where the bottom 10 Å of the substrate is frozen. The rigid indenter has Berkovich shape with equilateral triangular sides that are 204 Å long and the height is 28 Å. (This indenter shape is frequently used in the experimental studies of nanoindentation.) The interaction between the atoms in the indenter and those in the substrate is made purely repulsive.

Initially, the indenter is placed 10 Å above the top surface of the substrate. The indenter is inserted up to 10% of the substrate thickness at an average velocity of 8.33 m/s,

^{a)}Electronic mail: anakano@usc.edu.

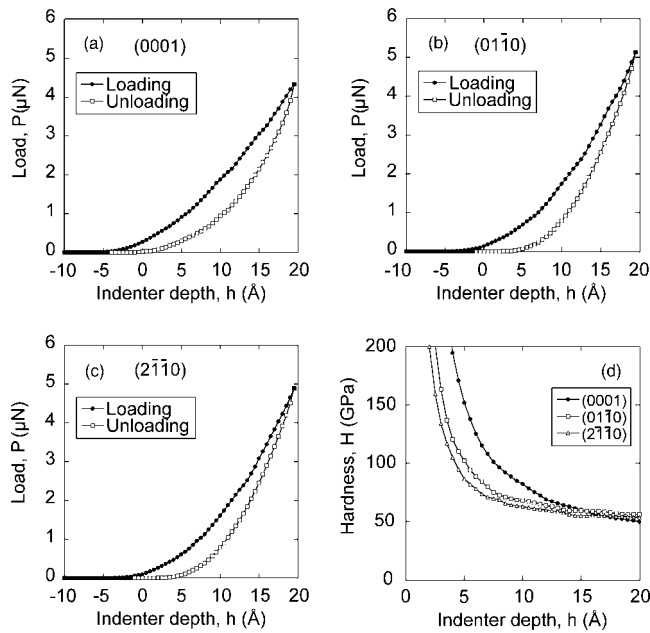


FIG. 1. Load-displacement curves for the (a) (0001), (b) (01 $\bar{1}0$) and (c) (2 $\bar{1}\bar{1}0$) indentations, and (d) hardness as a function of indentation depth.

where each 0.5 \AA change of the indenter position is followed by a holding phase of 6 ps to allow the decay of transient forces. The temperature of the system is maintained at 300 K by means of Nosé–Hoover method. The load P is calculated as the indenter-direction component of the force exerted on the indenter atoms averaged over the last 0.1 ps of the holding phase. The indenter depth h is calculated as the distance between the indenter tip and the initial thin film surface.

The calculated load-displacement curves for the (0001) basal, (01 $\bar{1}0$) prism, and (2 $\bar{1}\bar{1}0$) prism plane are shown in Figs. 1(a)–1(c), respectively. When the indenter approaches the surface, the indenter tip starts to interact with the thin film surface, and the load monotonically increases as a function of h , until the maximum depth is reached (see the solid circles). During the subsequent unloading phase with decreasing indenter depth, the load monotonically decreases and finally returns to zero (open squares). The hardness H is calculated as the load P divided by the projected area of the indenter. For Berkovich indenter, the projected area A is estimated as $A=3\sqrt{3}h^2 \tan^2 \theta$, where $\theta=63.5^\circ$ is the apex semi-angle of the indenter. Figure 1(d) shows the hardness as a function of h estimated from the data in Figs. 1(a)–1(c). For each plane, the hardness decreases with increasing indentation depth, which is in agreement with experimentally observed indentation size effects.^{5,7} The calculated hardness at the maximum indenter depth is approximately 50 GPa, which is likely to approach the experimental value for the (0001) basal plane, 39 GPa,³ at larger depths. Figure 1(d) also shows large anisotropy of the hardness value below $h \sim 15 \text{\AA}$.

To quantify the extent of plastic deformations, we show in Fig. 2 the number of disordered atoms, which are defined as aluminum atoms whose coordination number is different from that in the perfect crystal, as a function of h . For each plane, the number of disordered atoms is almost zero for $h < 2 \text{\AA}$, indicating the absence of defects in the film. The number of disordered atoms then rapidly increases as a function of h and, consequently, $h=2 \text{\AA}$ is considered as the yield

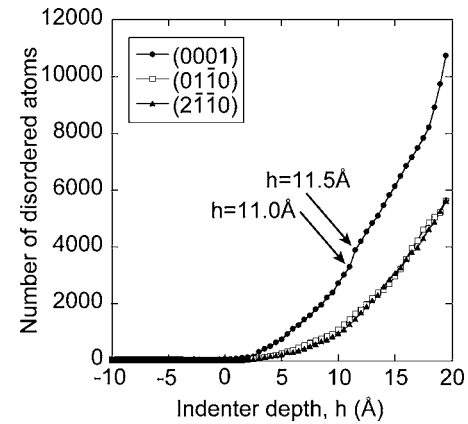


FIG. 2. Number of disordered aluminum atoms as a function of the indenter depth for (0001), (01 $\bar{1}0$), and (2 $\bar{1}\bar{1}0$) indentations.

point, i.e., the starting point of plastic deformation processes. Figure 2 shows more rapid increase in the number of disordered atoms for the basal plane, indicating more plastic deformation activities, than those for the prism planes.

To more closely examine plastic deformation processes for the (0001) basal plane indent, Figs. 3(a)–3(c) show snapshots of the atomic configuration under the indenter at $h=11.0$, 11.5, and 19.5 \AA (maximum indenter depth), respectively, where only disordered atoms are displayed. In Fig. 3(a), we observe three prism dislocations emitted from the three sides of the Berkovich indenter in the direction perpendicular to the surface. Stacking faults are formed in each of the prism planes because the prism dislocations are extended to the Shockley partial dislocations. Because the prism dislocations glide in the prism planes, accompanied by the expansion of stacking faults until the indenter depth reaches 11.0 \AA , the number of disordered atoms increases with increasing h , as shown in Fig. 2. At $h=11.5 \text{\AA}$, basal and pyramidal dislocations are generated. This explains the sudden increase in the number of disordered atoms between $h=11.0$ and 11.5 \AA in Fig. 2, indicating changes in deformation mechanisms. In Fig. 3(b), we observe basal and pyramidal dislocations, as well as stacking faults in both the basal and pyramidal planes caused by the expansion of the basal and pyramidal dislocations. The number of emitted basal dislocations is greater than those of the other dislocations because the elastic energy per unit length of the basal dislocation is less than those for other dislocations according to the theoretical analysis. These simulation results are consistent with experimental TEM data, in which these three kinds of dislocations have been observed.^{18,19}

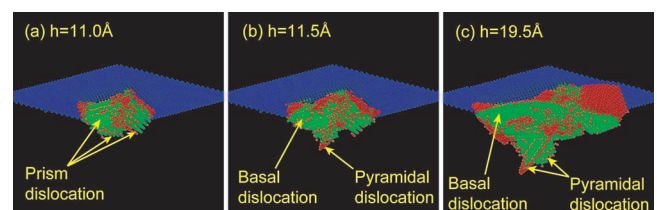


FIG. 3. (Color) Disordered aluminum atoms beneath the indenter for (0001) indentation at indenter depth of (a) 11.0 \AA , (b) 11.5 \AA , and (c) 19.5 \AA . Blue, red, and green colors represent coordination number of 3, 4, and 5, respectively. Note that the coordination number of an aluminum atom is 6 in an α -alumina crystal.

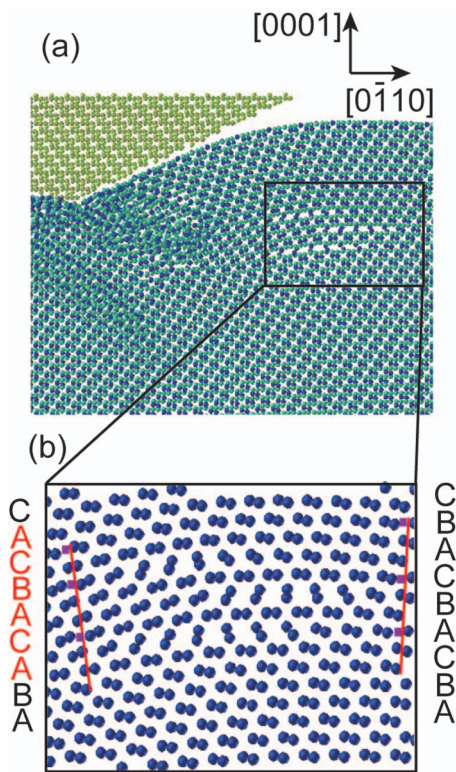


FIG. 4. (Color) (a) A snapshot of the atomic configuration under the indenter at indenter depth of 19.5 Å. Blue and cyan spheres are aluminum and oxygen atoms, respectively, whereas yellow spheres are indenter atoms. (b) Magnification of the rectangular region in (a). Only aluminum atoms are displayed as blue spheres. The stacking orders along the red lines are denoted by capital letters, and purple spheres indicate unoccupied lattice sites.

Figure 4 shows snapshots of the atomic configuration at the maximum indenter depth ($h=19.5$ Å) for the (0001) basal indent. In Fig. 4(a), blue and cyan spheres are aluminum and oxygen atoms, respectively, whereas yellow spheres are indenter atoms. We see surface bending due to indentation. The rectangular region in Fig. 4(a) is magnified in Fig. 4(b), where only aluminum atoms are displayed. At the central region in Fig. 4(b), the atomic configuration is disordered. The stacking orders along the red lines on both left and right sides of the disordered region are denoted by capital letters, and purple squares indicate unoccupied lattice sites. In a perfect α -alumina crystal, the stacking order of aluminum atoms is ABCABC..., as shown on the right hand side of Fig. 4(b). The stacking order of the left hand side of the disordered region deviates from that in the perfect α -alumina crystal, as shown in Fig. 4(b). This indicates that a leading partial dislocation exists at the center in Fig. 4(b) and the stacking fault is formed on the left hand side of the partial dislocation.

Figures 5(a) and 5(b) show plastic deformation processes for the two prism plane indents corresponding to the (0110) and (2110) planes, respectively, where only disordered aluminum atoms are shown. In case of the (0110) indent, two prism dislocations are emitted perpendicular to the indented surface. In contrast, in the case of the (2110) indent, a pyramidal dislocation is observed beneath the indenter.

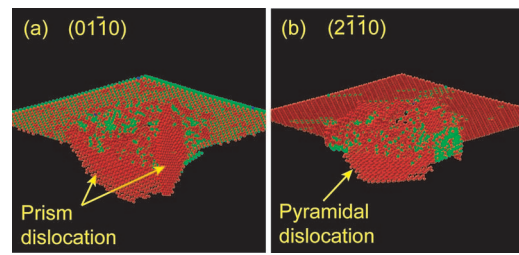


FIG. 5. (Color) Disordered aluminum atoms beneath the indenter at indenter depth of 19.5 Å for the (a) (0110) and (b) (2110) indentations.

In summary, we have performed MD simulations to study nanoindentation on a basal plane and two prism planes of an α -alumina crystal to examine the influence of surface orientation on plastic deformation processes. The hardness value estimated from the calculated load-displacement responses exhibits significant anisotropy and indentation size effect. Through careful analyses, we have attributed the anisotropy to distinct plastic deformation processes under the indenter due to the activation of different slip systems for different indentation surfaces. It should be possible to observe such nanoindentation hardness anisotropy using ultrafine AFM tips.²⁰

This work was partially supported by ARO, DTRA, DOE-BES, DOE-SciDAC, and NSF-ITR.

- ¹W. C. Oliver and G. M. Pharr, *J. Mater. Res.* **7**, 1564 (1992).
- ²T. F. Page, W. C. Oliver, and C. J. McHargue, *J. Mater. Res.* **7**, 450 (1992).
- ³T. Scholz, G. A. Schneider, J. Munoz-Saldana, and M. V. Swain, *Appl. Phys. Lett.* **84**, 3055 (2004).
- ⁴Similar nanoscale ductility has been observed in other brittle materials such as glass, see F. Celarie, S. Prades, D. Bonamy, L. Ferrero, E. Bouchaud, C. Guillot, and C. Marliere, *Phys. Rev. Lett.* **90**, 075504 (2003).
- ⁵A. Krell and S. Schadlich, *Mater. Sci. Eng., A* **307**, 172 (2001).
- ⁶N. I. Tymiak, A. Daugela, T. J. Wyrobek, and O. L. Warren, *Acta Mater.* **52**, 553 (2004).
- ⁷S. J. Bull, T. F. Page, and E. H. Yoffe, *Philos. Mag. Lett.* **59**, 281 (1989).
- ⁸G. Alcalá, P. Skeldon, G. E. Thompson, A. B. Mann, H. Habazaki, and K. Shimizu, *Nanotechnology* **13**, 451 (2002).
- ⁹D. W. Brenner, S. B. Sinnott, J. A. Harrison, and O. A. Shenderova, *Nanotechnology* **7**, 161 (1996).
- ¹⁰C. L. Kelchner, S. J. Plimpton, and J. C. Hamilton, *Phys. Rev. B* **58**, 11085 (1998).
- ¹¹J. Li, K. J. Van Vliet, T. Zhu, S. Yip, and S. Suresh, *Nature (London)* **418**, 307 (2002).
- ¹²E. T. Lilleodden, J. A. Zimmerman, S. M. Foiles, and W. D. Nix, *J. Mech. Phys. Solids* **51**, 901 (2003).
- ¹³D. Feichtinger, P. M. Derlet, and H. Van Swygenhoven, *Phys. Rev. B* **67**, 024113 (2003).
- ¹⁴P. Walsh, R. K. Kalia, A. Nakano, P. Vashishta, and S. Saini, *Appl. Phys. Lett.* **77**, 4332 (2000).
- ¹⁵P. Walsh, A. Omeltchenko, R. K. Kalia, A. Nakano, P. Vashishta, and S. Saini, *Appl. Phys. Lett.* **82**, 118 (2003).
- ¹⁶I. Szlufarska, R. K. Kalia, A. Nakano, and P. Vashishta, *Appl. Phys. Lett.* **85**, 378 (2004).
- ¹⁷I. Szlufarska, R. K. Kalia, A. Nakano, and P. Vashishta, *Appl. Phys. Lett.* **86**, 021915 (2005).
- ¹⁸B. J. Hockey, *J. Am. Ceram. Soc.* **54**, 223 (1971).
- ¹⁹S. J. Lloyd, J. M. Molina-Aldareguia, and W. J. Clegg, *Philos. Mag. A* **82**, 1963 (2002).
- ²⁰M. Ternes, C. P. Lutz, C. F. Hirjibehedin, F. J. Giessibl, and A. J. Heinrich, *Science* **319**, 1066 (2008).